22nd Australasian Fluid Mechanics Conference AFMC2020
Brisbane, Australia, 7–10 December 2020
https://doi.org/10.14264/ad70392

Active and inactive motions in wall turbulence

Rahul Deshpande, Jason P. Monty and Ivan Marusic

Department of Mechanical Engineering, University of Melbourne, Parkville, VIC 3010, Australia

Abstract

Reynolds shear stress is the key momentum transport term in wall turbulence and as a consequence has been the focus of numerous theoretical modelling attempts in the past. Here, we investigate the seminal proposal by Townsend [35, 34] that wall-bounded flows are comprised of active and inactive motions; the active motions being those that are solely responsible for producing Reynolds shear stress and follow self-similarity when normalised with the wall-normal distance and friction velocity. This paper builds on the recent work of Deshpande et al. [12], where a methodology is proposed to segregate the active and inactive contributions to the total turbulent kinetic energy. The effectiveness of this methodology is demonstrated here by applying it to three published wall-turbulence datasets, spanning over a decade change in friction Reynolds number (Re_τ). Active contributions to the streamwise, spanwise and wall-normal turbulence intensities are estimated individually and found to exhibit self-similar characteristics consistent with Townsend's hypothesis. The Reynolds shear stress, estimated solely from the active contributions, is also found to closely match the one obtained conventionally from the dataset, providing direct empirical support for the concept of active and inactive motions.

Keywords
Turbulent boundary layers; Boundary layer structure; Turbulence modelling

Introduction

The logarithmic (log) region of a wall-bounded flow has long been the focus of research from the perspective of turbulence modelling. It derives its name from the logarithmic variation of the mean velocity (U) as a function of the distance from the wall, z, following:

$$U^+ = \frac{1}{\kappa}\log(z^+) + A. \tag{1}$$

Here, $U^+ = U/U_\tau$, where U_τ is the friction velocity, $z^+ = zU_\tau/\nu$, where ν is the kinematic viscosity, κ is the von Kármán constant, and A is a constant. While (1) has been derived from a number of previous approaches, starting from the mixing length theory of Prandtl [30], the present manuscript focuses on the arguments proposed by Townsend [35, 34] in the context of the log-region, which he referred to as the 'equilibrium layer.' Townsend considered the local rates of energy production and dissipation to be in balance in this region, leading him to the same expression as that reached by Prandtl [30]:

$$-\overline{uw}^+ = l_m U_\tau \frac{dU^+}{dz^+}, \tag{2}$$

were, l_m is the mixing length. Throughout this paper, we denote the velocity fluctuations along streamwise (x), spanwise (y) and wall-normal (z) directions by u, v and w, respectively. $\overline{uw}^+$, is the (kinematic) Reynolds shear stress. Equation (2) leads to the log-law (1) when $l_m = \kappa z$ and -$\overline{uw}^+$ = 1. Townsend [35] interpreted this condition ($l_m \propto z$) in a physical sense in terms of an attached eddy: "*if the Reynolds stress at any point were caused mostly by contributions from eddies whose scales are comparable with distance of the point from the wall since they all extend to the wall and are, in a sense, attached to it.*"

The aforementioned arguments laid the foundation of Townsend's attached eddy hypothesis [34], from which the attached eddy model (AEM) of wall turbulence [28, 21] has evolved over time. The term 'attached' used here refers to any flow structure whose geometric lengths scale with z, respectively. The AEM conceptually models the kinematics in the log-region of a canonical wall-bounded flow by a hierarchy of randomly distributed, geometrically self-similar attached eddies, with a population density inversely proportional to their height ($\mathcal{H}$). According to Townsend [34], the heights of the attached eddies can vary in the range $O(z_l) \lesssim \mathcal{H} \lesssim O(\delta)$, with δ corresponding to the characteristic outer scale of the wall-bounded flow while z_l corresponding to the start of the log-region. In addition to complying with the log-law given in (1), the AEM also proposes the streamwise ($\overline{u^2}$) and spanwise ($\overline{v^2}$) turbulence intensities, resulting from the combined contributions from all attached eddies, to vary logarithmically with respect to the distance from the wall (z) in the log-region, while the variance of the wall-normal velocity ($\overline{w^2}$) remains constant. This can be expressed mathematically as:

$$\begin{aligned} \overline{u^2}^+ &= B_1 - A_1 \log\left(\frac{z}{\delta}\right), \\ \overline{v^2}^+ &= B_2 - A_2 \log\left(\frac{z}{\delta}\right), \\ \overline{w^2}^+ &= B_3, \text{ and } \overline{uw}^+ = B_4, \end{aligned} \tag{3}$$

where A_{1-3} and B_{1-3} are constants. These expressions have received substantial support in the recent literature from experiments [13, 22, 4] as well as simulations [15, 18, 26].

Considering the differing trends amongst the Reynolds stresses in (3), where the variances of the wall-parallel velocity components vary with Re_τ at a fixed z^+, while $\overline{w^2}^+$ and $\overline{uw}^+$ do not, Townsend [35] commented that: "*it is difficult to reconcile these observations without supposing that the motion at any point consists of two components, an active component responsible for turbulent transfer and determined by the stress distribution and an inactive component which does not transfer momentum or interact with the universal component.*" He further added "*that the inactive motion is a meandering or swirling motion made up from attached eddies of large size which contribute to the Reynolds stress much further from the wall than the point of observation*". The present manuscript further elaborates on these interpretations by presenting a simple mathematical description, combined with appropriate empirical support, for the concept of active and inactive motions.

For this, we begin by considering the simplest attached eddy model for a wall-bounded flow [7], comprising attached eddies as the only eddying motions. Figure 1(a) schematically depicts the signatures of all three velocity components from a simplified vortex structure, which is representative of an attached eddy of height $\mathcal{H}$. Given the inviscid nature of the model, slip is allowed at the wall (i.e. a finite u and v), while $w = 0$ due to the

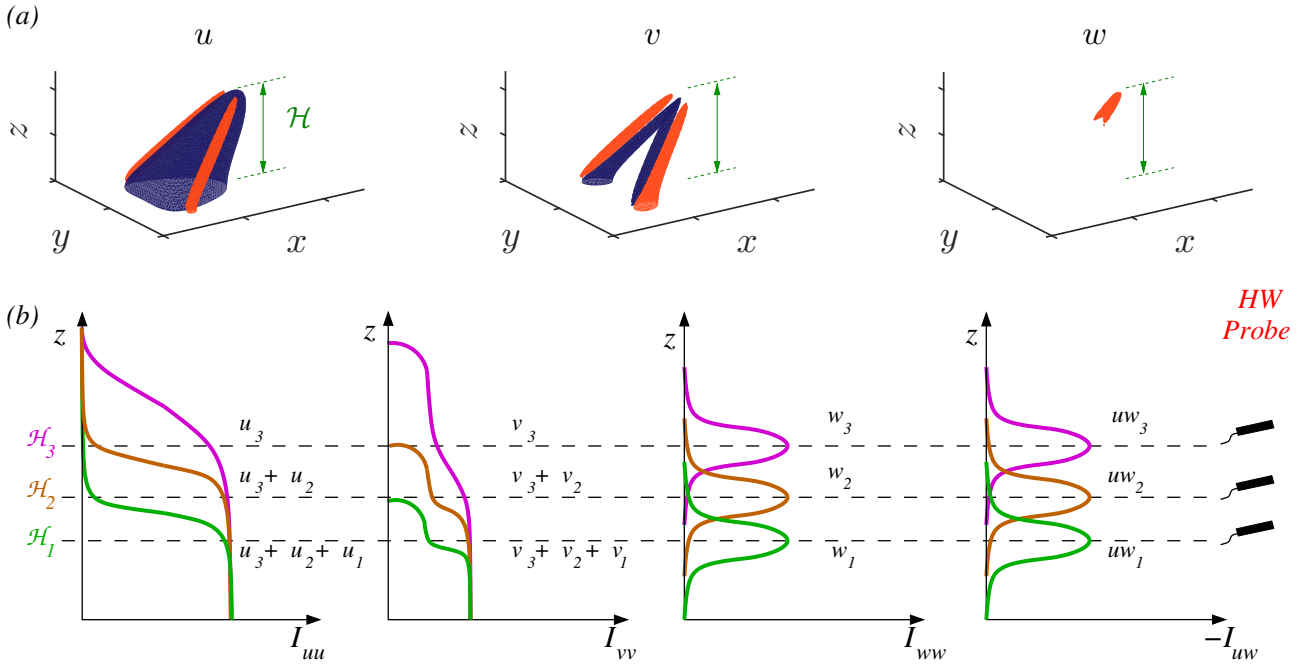

Figure 1. (a) Streamwise, spanwise and wall-normal velocity signatures from a typical attached eddy of height $\mathcal{H}$, where the blue and red regions denote the low- and high-momentum regions for the corresponding velocity fluctuations. (b) Townsend eddy intensity functions (I) for attached eddies of three different heights $\mathcal{H}_i$, with $\mathcal{H}_1 < \mathcal{H}_2 < \mathcal{H}_3$. Here, u_i, v_i and w_i denote the velocity signatures from the corresponding attached eddies which are sensed by the hotwire (HW) probe depending on its wall-normal position z, indicated by a dash line.

impermeability condition at the wall. This is ensured by using an image vortex about the plane of the wall. The final result is that the u- and v- signatures are present all the way from $\mathcal{H}$, down to the wall, while the w-signature remains spatially localized at $\mathcal{H}$. It is this very nature of the velocity signatures which results in the 'active' and 'inactive' contributions from the individual attached eddies, as will be explained below.

To highlight the difference between the two contributions, figure 1(b) depicts the Townsend eddy intensity function, I_{ij} (where i, $j = u$, v or w), which represents the contribution of each eddy to the individual turbulence stresses as a function of z [28, 21]. Here, I_{ij} is considered for the Reynolds stresses listed in (3), for eddies of three different heights ($\mathcal{H}_1$–$\mathcal{H}_3$), each symbolic of a hierarchy of attached eddies as per Townsend's hypothesis. The intensity functions associated with the normal stresses (I_{ii}) are representative of the corresponding velocity signatures depicted in figure 1(a). Using these functions, figure 1(b) depicts the cumulative contribution from the three different eddies to the Reynolds stresses measured by a hotwire probe. For the probe positioned at $z \sim \mathcal{H}_1$ for example, contributions to $\overline{u^2}(z)$ and $\overline{v^2}(z)$ would come from all three eddies, while the contributions to $\overline{w^2}(z)$ (and consequently to $\overline{uw}$) would be solely from the eddy of height $\mathcal{H}_1$. On increasing the probe wall-normal location to $z \sim \mathcal{H}_2$, contributions to the wall-parallel stresses now come from the tallest two eddies while those to $\overline{w^2}(z)$ and $\overline{uw}(z)$ would only be from the eddy of height $\mathcal{H}_2$, and so on. Correlating the observations from figure 1 with Townsend's definition, the active motions at any z would thus correspond solely due to the attached eddies of height, $\mathcal{H} \sim O(z)$. On the other hand, the inactive motions at z are a consequence of comparatively taller and larger attached eddies of height $O(z) \ll \mathcal{H} \lesssim O(\delta)$. Such attached eddies add to $u(z)$ and $v(z)$ without making any substantial addition to $w(z)$ (and thus to $uw(z)$). Therefore, while only active motions contribute to the Reynolds shear stress and the wall-normal velocity variance at z, the wall-parallel velocity variances receive contributions from both active and inactive motions. As a consequence, the active motions are defined as the fraction of attached eddy contributions which exhibit scaling with z and U_τ (i.e. wall-scaling). The logarithmic decay of the wall-parallel velocity variances (equation 3), on the other hand, is a consequence of the comparatively large scale inactive motions with a population density inversely proportional to their size.

The aforementioned discussion motivates the decomposition of the attached eddy fields as per Panton [27]:

$$\begin{aligned} u &= u_{\text{active}} + u_{\text{inactive}}, \\ v &= v_{\text{active}} + v_{\text{inactive}}, \\ w &= w_{\text{active}}. \end{aligned} \tag{4}$$

Given that the active and inactive velocity fields are uncorrelated [35, 5], the Reynolds stresses in (3) can also be decomposed as:

$$\begin{aligned} \overline{u^2} &= \overline{u^2}_{\text{active}} + \overline{u^2}_{\text{inactive}}, \\ \overline{v^2} &= \overline{v^2}_{\text{active}} + \overline{v^2}_{\text{inactive}}, \\ \overline{w^2} &= \overline{w^2}_{\text{active}}, \\ \overline{uw} &= \overline{(u_{\text{active}})(w_{\text{active}})} = \overline{(u_{\text{active}})(w)}. \end{aligned} \tag{5}$$

This decomposition is based on neglecting the non-linear interactions (like modulation) across these motions known from previous studies [24, 23, 20, 6, 36]. These interactions, however, do not show up in the second-order velocity statistics (i.e., the Reynolds stresses), which are of prime interest in the present work.

While (4) and (5) provide a mathematical description of the active and inactive contributions to the total energy, they have been defined considering a pure attached eddy field. A real

Flow	Channel		ZPG TBL		ZPG TBL	
$Re_\tau \approx$	934		2 000		14 000	
Dataset	del Alamo et al. [8]		Sillero et al. [32]		Deshpande et al. [10, 12]	
Symbol	$\mathcal{C}_1$		$\mathcal{B}_1$		$\mathcal{B}_2$	
$Set-up$	z_o^+	z_r^+	z_o^+	z_r^+	z_o^+	z_r^+
Φ_{ii}	**15**, $2.6\sqrt{Re_\tau} - 0.15Re_\tau$	$= z_o^+$	**15**, $2.6\sqrt{Re_\tau} - 0.15Re_\tau$	$= z_o^+$	**15**, $2.6\sqrt{Re_\tau} - 0.15Re_\tau$	$\approx z_o^+$
Φ_{ii}^{cross}	$2.6\sqrt{Re_\tau} - 0.15Re_\tau$	**15**	$2.6\sqrt{Re_\tau} - 0.15Re_\tau$	**15**	$2.6\sqrt{Re_\tau} - 0.15Re_\tau$	**15**

Table 1. Table summarizing the various published wall-turbulence datasets, with synchronized multi-point velocity signals across several z_r^+ and z_o^+, utilized to estimate two different types of two-dimensional spectra, Φ_{ii} and Φ_{ii}^{cross}. Terminology used in the table has been defined in the text, where i represents the velocity fluctuations u, v or w. Highlighted values (in bold) are used to indicate the reference location close to the wall, while $2.6\sqrt{Re_\tau}$ and $0.15Re_\tau$ are the lower and upper bounds of the log-region [22]. Normalization in viscous units is denoted by the superscript '+'.

wall-bounded flow, however, also comprises of other 'non-self-similar' contributions [1, 10, 37], which also need to be recognized and correctly accounted for while considering these decompositions. These include the small-scale energy contributions from the inertial sub-range [29, 31], as well as those corresponding to the fine dissipative scales, which are small compared to the inertial motions in the log-region. Other contributions come from the δ-scaled superstructures or very-large-scale motions, which add to $\overline{u^2}$ and $\overline{v^2}$ [1, 10, 37] but not to $\overline{w^2}$, the latter being confirmed by the w-velocity energy spectra exhibiting wall-scaling [5, 25, 16, 17, 3]. These characteristics suggest the δ-scaled superstructure behaviour to be aligned with the inactive motions, meaning their contributions would end up in $\overline{u^2}_{\text{inactive}}$ and $\overline{v^2}_{\text{inactive}}$ [12] in the context of the decomposition given in (5).

Recently, Deshpande et al. [12] proposed a methodology to segregate $\overline{u^2}_{\text{inactive}}$ and $\overline{u^2}_{\text{active}}$ in the logarithmic layer of a zero pressure gradient turbulent boundary layer (ZPG TBL). The present manuscript reviews their methodology, and demonstrates its applicability to decompose the inactive and active contributions for all three velocity components, and for canonical wall-bounded flows in general. The methodology utilizes the characteristic of the inactive motions, say at any z_o in the log-region, to be associated predominantly with the large eddies in comparison to the motions 'active' at the same location, which means the coherence of the inactive motions extends across a significant wall-normal distance [34, 1]. This is consistent with Townsend's ideas [35, 34], who described the inactive motions (at z_o) to be superimposing a low-frequency signature across the entire wall-normal range below z_o, including the near-wall region [14] where we consider our reference location, z_r. The presence of their signatures across the large wall-normal range ($z_r \ll z_o$) provides an opportunity to isolate the inactive motions via a scale-specific cross-correlation of the velocity signals synchronously acquired at z_r and z_o, as demonstrated previously in Refs [11, 1]. Once the inactive component is estimated ($\overline{v^2}_{\text{inactive}}$ or $\overline{u^2}_{\text{inactive}}$), it can be simply subtracted from the respective Reynolds stress at z_o ($\overline{v^2}$ or $\overline{u^2}$) to estimate the energy associated with the active motions at z_o (equation 5). In the case of the wall-normal component, however, $\overline{w^2}_{\text{inactive}} \approx 0$ as per our earlier discussion [12], and hence $\overline{w^2}$ should reflect the characteristic features expected of $\overline{w^2}_{\text{active}}$ [5, 25, 16, 17, 3].

To demonstrate the efficacy of the decomposition methodology, several published wall-turbulence datasets with synchronized multi-point velocity signals measured across a large domain of spanwise (Δy) and wall-normal ($|z_r - z_o|$) offsets are considered. The data spans over a decade of Re_τ, with the velocity signals in each dataset considered across the log-region of the shear flow, making it possible to test the velocity spectra associated with the active motions for their expected wall-scaling. The methodology involves first computing the two-dimensional (2-D) energy spectrum from the available velocity components at z_o and z_r, thereby giving a map of the energetic motions of various spanwise ($\lambda_y = 2\pi/k_y$) and streamwise ($\lambda_x = 2\pi/k_x$) wavelengths coherent across z_r and z_o [10]. These two-point statistics, can be utilized in conjunction with a spectral linear stochastic estimation (SLSE) based procedure [33, 2, 12], to compute the fraction of the two-dimensional spectrum (at z_o) corresponding to the inactive motions at z_o.

Experimental and numerical data

Three published datasets ranging over a decade of Re_τ are analyzed in the present study. Two are low Re_τ direct numerical simulation (DNS) datasets for the turbulent channel flow ($Re_\tau \approx$ 934;[8]) and the ZPG TBL ($Re_\tau \approx$ 2 000;[32]), while the third is a high Reynolds number ($Re_\tau \approx$ 14 000) experimental dataset for the ZPG TBL [10, 12]. Information associated with these datasets is briefly described below.

High Re_τ experimental dataset

The experimental dataset ($\mathcal{B}_2$) was acquired in the High Reynolds Number Boundary Layer Wind Tunnel (HRNBLWT) at the University of Melbourne under nominally ZPG conditions and acceptable free-stream turbulence levels [19] across its test section dimensions of $\simeq 1.89$ m $\times$ 0.92 m $\times$ 27 m. All the measurements associated with the present dataset were conducted at free-stream velocities of $U_\infty \approx 20$ ms^{-1} in the working section, at a streamwise location approximately 20 m from the beginning of the working section, resulting in a boundary layer at $Re_\tau \approx 14\,000$. The experiments were conducted via a unique experimental set-up employing four single-wire hotwire probes, the positioning of which has been depicted schematically in figure

1 of Refs [10, 12]. The set-up consisted of all four probes positioned at the same streamwise location but at different spanwise positions, with the capability to vary the latter for two of the four probes. This facilitated synchronous measurement of the u-signals over a large domain of spanwise offsets (Δy), ranging between $0 \lesssim \Delta y \lesssim 2.7\delta$, where δ is the TBL thickness. During each experiment, the pair of spanwise-traversing probes were always positioned at the same wall-normal location z_o, while the pair of spanwise-fixed probes were maintained at a different wall-normal position, z_r. The synchronous u-signals acquired from such an arrangement is utilized to compute the two-point cross-correlation following:

$$R_{i_o i_r}(z_o, z_r; \Delta x, \Delta y) = \overline{i(z_o; x+\Delta x, y+\Delta y) i(z_r; x, y)}, \quad (6)$$

with the overbar denoting ensemble time average, and $i = u$ in case of the experimental dataset. $R_{i_o i_r}$ is converted from a function of time to that of Δx by using Taylor's hypothesis, which assumes flow structures coexisting at z_o to be moving along x at the mean flow velocity at z_o. Subsequently, the 2-D Fourier transform of $R_{i_o i_r}$ is computed to obtain the 2-D spectrum following:

$$\phi_{i_o i_r}(z_o, z_r; k_x, k_y) = \int\int_{-\infty}^{\infty} R_{i_o i_r}(z_o, z_r; \Delta x, \Delta y) e^{-j2\pi(k_x \Delta x + k_y \Delta y)} d(\Delta x) d(\Delta y), \quad (7)$$

where j is a unit imaginary number.

The present study focuses on two types of 2-D spectra, Φ_{ii} and Φ_{ii}^{cross}, which are defined following:

$$\begin{aligned} \Phi_{ii}(z_o^+; \lambda_x, \lambda_y) &= |k_x^+ k_y^+ \phi_{i_o i_o}^+(z_o^+; \lambda_x, \lambda_y)| \text{ and} \quad (8) \\ \Phi_{ii}^{cross}(z_o^+, z_r^+; \lambda_x, \lambda_y) &= |k_x^+ k_y^+ \phi_{i_o i_r}^+(z_o^+, z_r^+ \approx 15; \lambda_x, \lambda_y)|, \end{aligned}$$

where i corresponds to the velocity fluctuations in either of the three directions: u, v or w, while $(||)$ denotes the modulus operation. While Φ_{ii} consists of contributions from all coexisting eddies at z_o, Φ_{ii}^{cross} is representative of contributions from only those eddies that are coherent across z_o and z_r [10]. The two spectra are fed in to the SLSE methodology [12] to compute the subsets of Φ_{ii} comprising of the inactive and active contributions at z_o. In the case of dataset $\mathcal{B}_2$, the analysis is solely restricted to Φ_{uu} and Φ_{uu}^{cross}, with the details of their wall-normal locations listed in table 1. Interested readers may refer to Refs [10, 12] for a comprehensive discussion and full details of the aforementioned measurements.

Low Re_τ DNS datasets

Two low Re_τ datasets from the ZPG TBL DNS of Sillero et al. [32] and channel flow DNS of del Alamo et al. [8] are also considered in the present study. Availability of all three velocity components from both these datasets allows computation of $\Phi_{ii}(z_o^+)$ and $\Phi_{ii}^{cross}(z_o^+, z_r^+)$ following (6) – (8) for $i = u$, v and w, at z_o^+ and z_r^+ consistent with the experimental dataset (table 1). Thirteen DNS time blocks of each of these datasets are selected for achieving a reasonable convergence of these statistics. Hence, in the present study, while the characteristics of the u-motions are tested across a decade of Re_τ, the analysis of the v- and w-motions is limited only to the low Re_τ regime.

Methodology to decompose inactive and active contributions to the total energy

As discussed previously in the introduction, the inactive motions at z_o predominantly conform to the large motions that are spatially coherent over a significant wall-normal distance. Deshpande et al. [12] used this as the basis to decompose $\Phi_{ii}(z_o)$. They performed a scale-specific linear decomposition of $\Phi_{ii}(z_o)$, into its inactive and residual component, by making use of the scale-by-scale coupling that exists between the velocity signals measured simultaneously at the two locations, $z_r^+ \approx 15$ and z_o^+ (in the log-region), such that $z_r^+ \ll z_o^+$. The scale-by-scale coupling is represented here in the form of Φ_{ii}^{cross}, which is considered at various z_o^+ for both the DNS as well as experimental datasets (table 1).

To give a qualitative indication of how Φ_{ii}^{cross} differs from Φ_{ii}, figures 2(a,c) show Φ_{uu}^{cross} and Φ_{uu} contours from the two ZPG TBL datasets at z_o^+ across the log-region as an example. It is evident that the former represents the large energetic motions associated with the inactive motions at z_o^+. Φ_{ii}^{cross} also comprises energy signatures from the very large-scale superstructures (scaling with δ), which are known to span across the entire log-region and extend all the way down to the wall [1, 10, 37]. These observations motivate the use of Φ_{ii}^{cross} in conjunction with the SLSE [33, 2, 12], to compute the linear stochastic estimate of the energy contributions (Φ_{ii}^{ia}) from the motions inactive at z_o following:

$$\Phi_{ii}^{ia}(z_o^+; \lambda_x, \lambda_y) = \frac{\left[\Phi_{ii}^{cross}(z_o^+, z_r^+ \approx 15; \lambda_x, \lambda_y)\right]^2}{\Phi_{ii}(z_r^+ \approx 15; \lambda_x, \lambda_y)}, \quad (9)$$

whereby $\Phi_{ii}^{ia}(z_o^+)$ is essentially a normalized version of $\Phi_{ii}^{cross}(z_o^+, z_r^+ \approx 15)$, with the scale-by-scale normalization done by $\Phi_{ii}(z_r^+ \approx 15)$. Readers interested to see the step-by-step procedure to arrive at the expression in (9) may refer to appendix 1 of Deshpande et al. [12]. It is important to note here that the calculations in (9), in case of the experimental dataset, are conducted in the frequency domain, and are later converted to λ_x by invoking Taylor's hypothesis, using the mean streamwise velocity at z_o as the convection velocity [2, 12]. In accordance to the linear superposition assumption in (5), subtracting Φ_{ii}^{ia} from Φ leaves a residual:

$$\Phi_{ii}^{a}(z_o^+; \lambda_x, \lambda_y) = \Phi_{ii}(z_o^+; \lambda_x, \lambda_y) - \Phi_{ii}^{ia}(z_o^+; \lambda_x, \lambda_y). \quad (10)$$

This is because for $i = u$, as an example, Φ_{uu}, Φ_{uu}^{a} and Φ_{uu}^{ia} are representative of $\overline{u^2}^+$, $\overline{u^2}^+_{\text{active}}$ and $\overline{u^2}^+_{\text{inactive}}$, respectively. If the flow comprised of only inactive and active inertial motions, Φ_{ii}^{ia} and Φ_{ii}^{a} would respectively be the inactive and active component. We, however, refer to Φ_{ii}^{a} as the residual spectrum, since it also consists of small energy contributions from the inertial sub-range as well as fine dissipative scales, apart from the more energetic active motions.

Figures 2(b,d) plots the constant energy contours for the two sub-components $\Phi_{uu}^{ia}(z_o^+)$ and $\Phi_{uu}^{a}(z_o^+)$, for the two ZPG TBL datasets at z_o^+ across the log-region as an example. These subsets have been estimated using (9) and (10), using the corresponding spectra shown in figures 2(a,c), respectively. While Φ_{uu}^{a} takes up the small-scale end of the spectrum, Φ_{uu}^{ia} is restricted to the large-scale portion of Φ. Figure 2 also shows the line $\lambda_y \sim \lambda_x$, which is indicative of geometric self-similarity. For the wall-normal location at the lower end (figure 2(b)) of the log-region, both $\Phi_{uu}^{a}(z_o^+)$ and $\Phi_{uu}^{ia}(z_o^+)$ nominally follow the $\lambda_y \sim \lambda_x$ line, while this is obscured for Φ_{uu}, in the intermediate and large-scale range [10]. The conformance of Φ_{uu}^{ia} and Φ_{uu}^{a} contours to the linear relationship is consistent with the hypothesis of Townsend [35, 34], who proposed both the inactive and active motions to be related to the self-similar attached eddy contributions. The two motions, however, correspond to different hierarchies of the attached eddies: while the active motions at z_o^+ are associated with the attached eddies of height, $\mathcal{H} \sim \mathcal{O}(z_o)$, the inactive motions conform to larger eddies of height $\mathcal{O}(z_o) \ll \mathcal{H} \lesssim \mathcal{O}(\delta)$. This explains why the contribution from

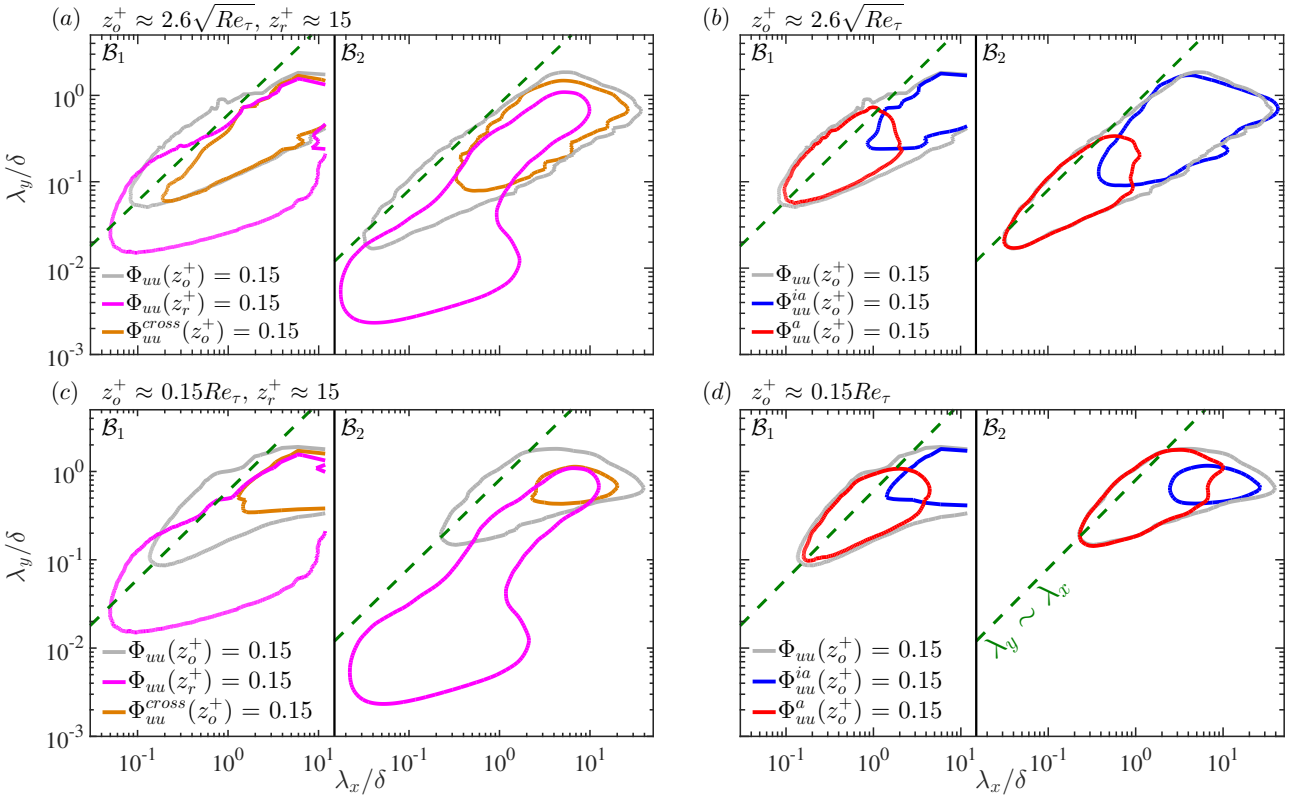

Figure 2. (a,c) Constant energy contours for $\Phi_{uu}(z_o^+)$, $\Phi_{uu}^{cross}(z_o^+, z_r^+ \approx 15)$ and $\Phi_{uu}(z_r^+ \approx 15)$ at energy level of 0.15 plotted for (a) $z_o^+ \approx 2.6\sqrt{Re_\tau}$ and (c) $z_o^+ \approx 0.15Re_\tau$. (b,d) Constant energy contours for $\Phi_{uu}^{ia}(z_o^+)$ and $\Phi_{uu}^{a}(z_o^+)$, computed via (9) and (10), plotted at the same energy level and z_o^+ as in (a,c), respectively. In (a-d), contours on the left and right side correspond to those computed from datasets $\mathcal{B}_1$ and $\mathcal{B}_2$, respectively. Dashed green lines represent the linear relationship, $\lambda_y \sim \lambda_x$. The figure has been adapted from Ref. [12].

the inactive motions to Φ_{uu}^{ia} reduces with increase in z_o^+ (figures 2(b,d)). In contrast, a substantial scale range is observed in the case of the Φ_{ii}^{a} contours irrespective of the increase in z_o^+, with the contours displaced to comparitively larger scales, which is indicative of its z_o-scaling. With the procedure to estimate Φ_{ii}^{a} and Φ_{ii}^{ia} now defined, next the spectra contours are tested for δ- and z_o-scaling to investigate the extent to which the respective contours relate with the characteristics of the inactive and active motions. Due to the limited availability of space here, the present analysis has been limited to active motions only. Interested readers are referred to Deshpande et al. [12] for a thorough analysis on both the inactive and active contributions.

Active motions

Figure 3 shows the constant energy contours of Φ_{ii}^{a} (for $i = u$, v or w), estimated for the three datasets at z_o^+ across the log-region. The contours are plotted as a function of wavelengths scaled with δ (figures 3(d-f)) as well as z_o (figures 3(a-c)). Given the exclusive association of the w-velocity component with the active motions [5, 25, 3, 12], i.e $\Phi_{ww} \approx \Phi_{ww}^{a}$, here we have directly considered the energy contours of Φ_{ww} for comparison. The residual component of each velocity spectrum can be noted to obey reasonable wall-scaling, which is evident from the overlapping Φ_{ii}^{a} contours plotted with the wavelengths scaled with z_o. On the other hand, no overlap can be noted in case of the wavelengths normalized by δ. The fact that the Φ_{ii}^{a} contours follow wall-scaling, reaffirms the efficacy of the present methodology to segregate the inactive and active contributions from the total energy, for all three velocity components in a wall-bounded flow. Further, the good agreement between Φ_{uu}^{a} (figure 3(a)) estimated from both the DNS and experimental datasets suggests the local mean streamwise velocity to be a reasonable choice for the convection velocity for the active motions.

The residual component of the 2-D spectra also conveys important information related to the geometric characteristics of the active motions, which may prove useful for future conceptual modelling efforts. Φ_{ii}^{a} contours, corresponding to all the velocity components, align along the linear relationship ($\lambda_y \sim \lambda_x$) which is indicative of geometric self-similarity. It suggests that the active motions can be conceptually modelled using Townsend's self-similar attached eddies. The results in figure 3 indicate that such an attached eddy should have its dominant streamwise/spanwise aspect ratios following $\lambda_x/\lambda_y \approx 3$ (for u), $\lambda_x/\lambda_y \approx 1.4$ (for w) and $\lambda_x/\lambda_y \approx 1$ (for v). Amongst these ratios, interestingly, the aspect ratio corresponding to the u-contributions closely relates with the self-similar wall-coherent vortex clusters ($\lambda_x \sim$ 2-3 λ_y) analyzed previously by del Alamo et al. [9] and Hwang [14]. This close agreement suggests the decomposition of Φ_{ii} into the two sub-components Φ_{ii}^{ia} and Φ_{ii}^{a}, comprising significant self-similar attached eddy contributions, and relating well to the two-component attached eddy structure hypothesized by Hwang [14].

Reynolds shear stress co-spectra

Townsend [35, 34] defined the active motions to be the sole Reynolds shear stress carrying motions at any z_o, with the co-existing inactive motions contributing negligibly to the shear stress at z_o. This means that the Reynolds shear stress co-spectra, which is defined as:

$$\Phi_{uw}(z_o^+;\lambda_x,\lambda_y) = \mathrm{Re}[k_x^+ k_y^+ \phi_{uw}^+(z_o^+;\lambda_x,\lambda_y)], \quad (11)$$

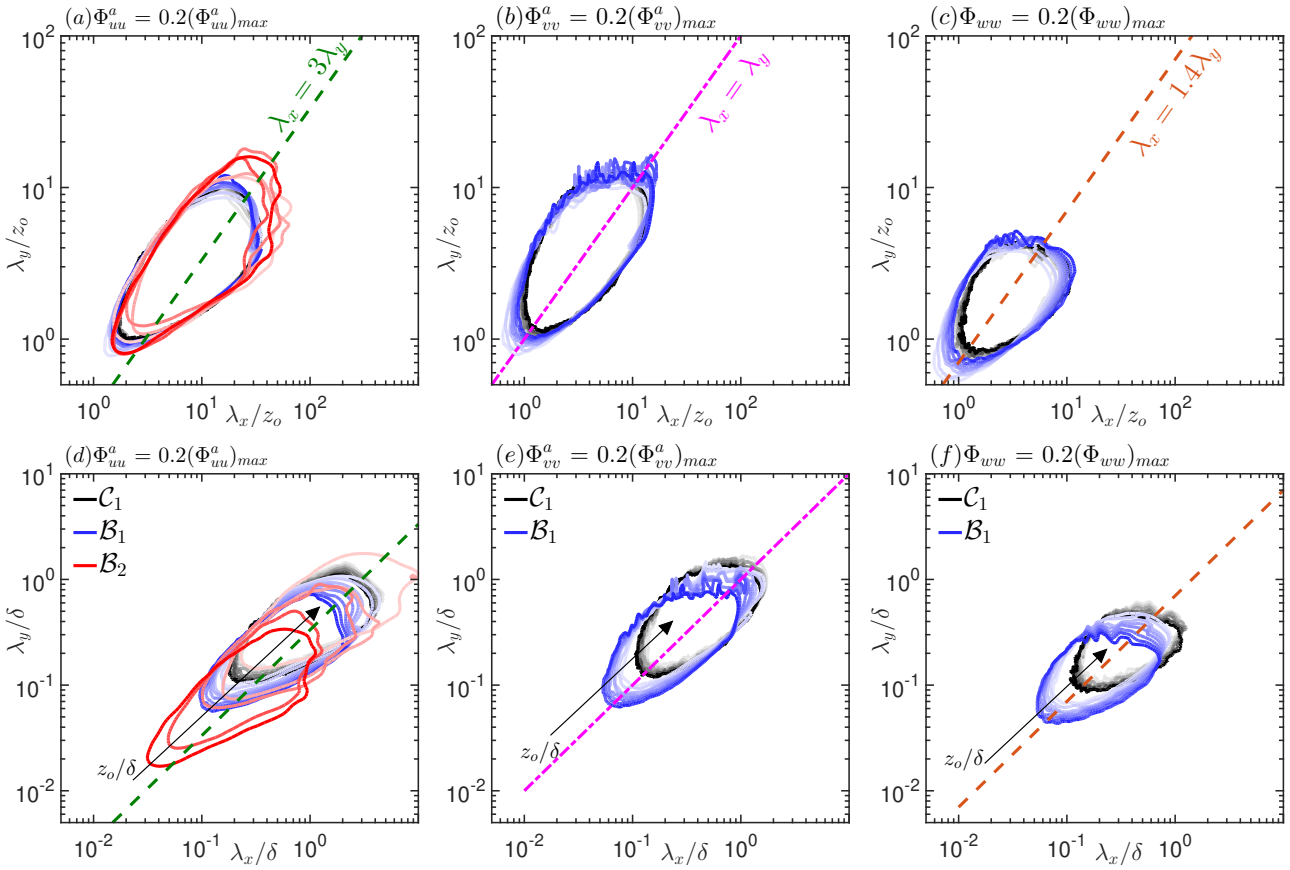

Figure 3. Constant energy contours for (a,d) $\Phi^a_{uu}(z_o^+)$, (b,e) $\Phi^a_{vv}(z_o^+)$ and (c,f) $\Phi_{ww}(z_o^+)$ ($\approx \Phi^a_{ww}(z_o^+)$) plotted for various z_o^+ as a function of wavelengths scaled with (a-c) z_o and (d-f) δ. Contours in black, blue and red correspond to $\Phi^a_{ii}(z_o^+)$ estimated for datasets $\mathcal{C}_1$, $\mathcal{B}_1$ and $\mathcal{B}_2$, respectively. Dark to light shading indicate an increase in z_o^+ following $2.6\sqrt{Re_\tau} \leq z_o^+ \leq 0.15Re_\tau$, for Re_τ corresponding to the respective datasets. Dashed green, magenta and brown lines represent the linear relationships empirically noted for Φ^a_{uu}, Φ^a_{vv} and Φ_{ww}, respectively.

should also exhibit wall-scaling [5, 25, 3], analogous to Φ_{ww} shown in figure 3. Here, Re refers to the real value of the complex-valued spectrum Φ_{uw}, which is estimated via cross-correlating the instantaneous velocity fluctuations, $u(z_o^+)$ and $w(z_o^+)$. While the former comprises of both the active (u_{active}) and inactive ($u_{inactive}$) contributions, it is u_{active} which contributes predominantly to Φ_{uw} as per Townsend's hypothesis [35, 34]. We test this here for the low Re_τ DNS data by separately estimating Φ^a_{uw}, defined as:

$$\Phi^a_{uw}(z_o^+;\lambda_x,\lambda_y) \quad = \quad \mathrm{Re}[k_x^+ k_y^+ \phi^+_{u_{active}w}(z_o^+;\lambda_x,\lambda_y)], \quad (12)$$

wherein Φ^a_{uw} is estimated by cross-correlating the active component of the instantaneous streamwise velocity, $u_{active}(z_o^+)$ and $w(z_o^+)$. To estimate the active and inactive contributions to the instantaneous flow field $u(z_o^+)$, we use the same SLSE methodology employed previously for segregating the two contributions to the energy spectrum. As per the SLSE methodology [2, 12]:

$$\widetilde{u}_{inactive}(z_o^+;\lambda_x,\lambda_y) = H_L(z_o^+, z_r^+{\approx}15;\lambda_x,\lambda_y)\widetilde{u}(z_r^+{\approx}15;\lambda_x,\lambda_y), \quad (13)$$

where $\widetilde{u}(z_r^+ \approx 15;\ \lambda_x,\ \lambda_y)$ is the 2-D Fourier transform of the instantaneous wall-parallel flow field, $u(z_r^+ \approx 15)$ in x and y. Here, H_L represents the scale-specific linear transfer kernel, and is estimated from an ensemble of data following:

$$H_L(z_o^+, z_r^+{\approx}15;\lambda_x,\lambda_y) = \frac{\langle \widetilde{u}(z_o^+;\lambda_x,\lambda_y)\widetilde{u}^*(z_r^+{\approx}15;\lambda_x,\lambda_y)\rangle}{\langle \widetilde{u}(z_r^+{\approx}15;\lambda_x,\lambda_y)\widetilde{u}^*(z_r^+{\approx}15;\lambda_x,\lambda_y)\rangle}, \quad (14)$$

where the asterisk ($*$) and angle brackets ($\langle\rangle$) denote the complex conjugate and ensemble averaging, respectively [12]. $u_{inactive}(z_o^+)$, which can be retrieved on inverse Fourier transforming $\widetilde{u}_{inactive}(z_o^+)$, is then used to obtain $u_{active}(z_o^+)$ following the linear decomposition of $u(z_o^+)$ given in (3).

Figure 4 compares Φ_{uw} and Φ^a_{uw} estimated for the two DNS datasets $\mathcal{B}_1$ (figure 4(b)) and $\mathcal{C}_1$ (figure 4(a)) at z_o^+ across the log-region. It can be observed that both Φ_{uw} and Φ^a_{uw} exhibit reasonable wall-scaling, with $\Phi_{uw} \approx \Phi^a_{uw}$ in the small and intermediate-scale range. The good overlap of contours in figure 4 is a testament to Townsend's hypothesis on the active motions being solely responsible for producing the Reynolds shear stress. There is, however, some disagreement between Φ_{uw} and Φ^a_{uw} at large scales, where Φ_{uw} contours can be seen deviating away from the z_o-scaling. This may be owing to the influence of the large δ-scaled motions via non-linear interactions with the active motions [24, 23], and is currently under investigation by the authors.

Conclusions

This paper presents arguments in support of Townsend's hypothesis [35, 34] on the statistical nature of the Reynolds stress carrying motions in wall-bounded turbulent flows. As per Townsend, the wall-bounded flow at any point comprises of two components – (i) active motions, which are responsible for transferring the momentum, and (ii) inactive motions, with both conforming to Townsend's self-similar attached eddies. Empirical support is provided to these arguments via implementation

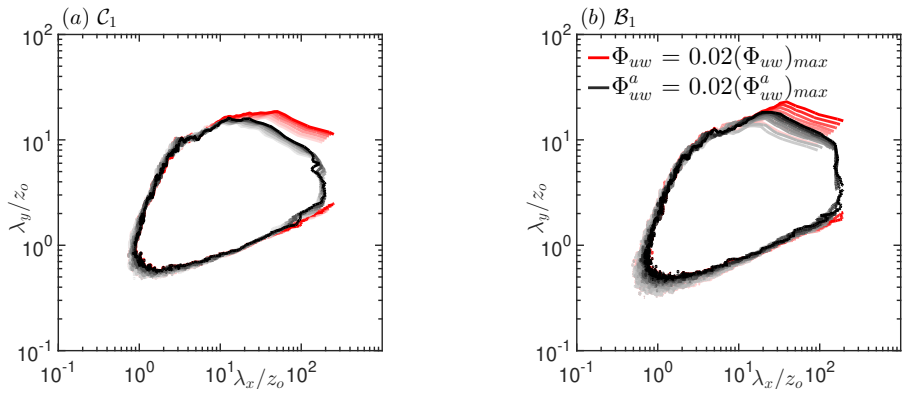

Figure 4. Constant energy contours for $\Phi_{uw}(z_o^+)$ (in red) and $\Phi^a_{uw}(z_o^+)$ (in black) computed for datasets (a) $\mathcal{C}_1$ and (b) $\mathcal{B}_1$ and plotted for various z_o^+ as a function of wavelengths scaled with z_o. Dark to light shading indicates an increase in z_o^+ following $2.6\sqrt{Re_\tau} \leq z_o^+ \leq 0.15Re_\tau$, for Re_τ corresponding to the respective datasets.

of an SLSE-based energy decomposition methodology on previously published wall-turbulence datasets. The procedure first isolates the turbulent kinetic energy associated with the inactive motions, by exploiting their known characteristic of being comparatively larger than the coexisting active motions [35, 34]. Energy associated with the active motions (Φ^a_{ii}, where $i = u$, v or w) is then estimated by subtracting this 'inactive' energy from the total energy.

The SLSE methodology is demonstrated to be effective for all three velocity components in a wall-bounded turbulent flow by testing the scaling characteristics of the active motions. Φ^a_{ii} contours are noted to obey wall-scaling across a large Re_τ range. The good overlap between the estimates from both the experimental and DNS datasets also establishes Taylor's hypothesis to be a reasonable assumption for the active motions. Further, the decomposition of Φ_{ii} into Φ^a_{ii} and Φ^{ia}_{ii} reveals the geometric self-similarity of the inactive and active motions, suggesting they can be conceptually modelled using the attached eddy model framework [28, 21]. The ability to decompose the active and inactive contributions also permits computation of Φ^a_{uw}, which considers the cross-correlation exclusively between u_{active} and w. Φ^a_{uw} contours are found to agree well with the Φ_{uw} contours, thus endorsing Townsend's hypothesis on the active motions as the sole Reynolds shear stress carrying motions in wall-bounded flows. In the present work, support towards the validity of Townsend's hypothesis, for the lateral velocity components, has only been possible via low-Re_τ datasets. This motivates undertaking of multi-component multi-point high Reynolds number experiments in the future to firmly establish the validity of this hypothesis for all three velocity components.

Acknowledgements

The authors wish to acknowledge the Australian Research Council for financial support and are thankful to the authors of Refs [8, 32] for making their respective data available. The authors also thank Drs Dileep Chandran, Woutijn Baars, Charitha de Silva and Anagha Madhusudanan for their valued support at various stages of this work.

References

[1] Baars, W. and Marusic, I., Data-driven decomposition of the streamwise turbulence kinetic energy in boundary layers. Part 1. Energy spectra, *Journal of Fluid Mechanics*, **882**, 2020, A25.

[2] Baars, W. J., Hutchins, N. and Marusic, I., Spectral stochastic estimation of high-Reynolds-number wall-bounded turbulence for a refined inner-outer interaction model, *Physical Review Fluids*, **1**, 2016, 054406.

[3] Baidya, R., Philip, J., Hutchins, N., Monty, J. P. and Marusic, I., Distance-from-the-wall scaling of turbulent motions in wall-bounded flows, *Physics of Fluids*, **29**, 2017, 020712.

[4] Baidya, R., Philip, J., Monty, J. P., Hutchins, N. and Marusic, I., Comparisons of turbulence stresses from experiments against the attached eddy hypothesis in boundary layers, in *Proceedings of 19th Australasan Fluid Mechanics Conference*, 2014.

[5] Bradshaw, P., 'Inactive' motion and pressure fluctuations in turbulent boundary layers, *Journal of Fluid Mechanics*, **30**, 1967, 241–258.

[6] Chernyshenko, S. I., Marusic, I. and Mathis, R., Quasi-steady description of modulation effects in wall turbulence, **arXiv:1203.3714 [physics.flu-dyn]**.

[7] de Silva, C., Kevin, K., Baidya, R., Hutchins, N. and Marusic, I., Large coherence of spanwise velocity in turbulent boundary layers, *Journal of Fluid Mechanics*, **847**, 2018, 161–185.

[8] del Álamo, J. C., Jiménez, J., Zandonade, P. and Moser, R. D., Scaling of the energy spectra of turbulent channels, *Journal of Fluid Mechanics*, **500**, 2004, 135–144.

[9] del Álamo, J. C., Jiménez, J., Zandonade, P. and Moser, R. D., Self-similar vortex clusters in the turbulent logarithmic region, *Journal of Fluid Mechanics*, **561**, 2006, 329–358.

[10] Deshpande, R., Chandran, D., Monty, J. and Marusic, I., Two-dimensional cross-spectrum of the streamwise velocity in turbulent boundary layers, *Journal of Fluid Mechanics*, **890**, 2020, R2.

[11] Deshpande, R., Monty, J. and Marusic, I., Streamwise inclination angle of large wall-attached structures in turbulent boundary layers, *Journal of Fluid Mechanics*, **877**, 2019, R4.

[12] Deshpande, R., Monty, J. and Marusic, I., Active and inactive components of the streamwise velocity in wall-bounded turbulence, *Journal of Fluid Mechanics (in press)*.

[13] Hultmark, M., Vallikivi, M., Bailey, S. C. C. and Smits, A. J., Turbulent pipe flow at extreme Reynolds numbers, *Physical Review Letters*, **108**, 2012, 094501.

[14] Hwang, Y., Statistical structure of self-sustaining attached eddies in turbulent channel flow, *Journal of Fluid Mechanics*, **767**, 2015, 254–289.

[15] Jimenez, J. and Hoyas, S., Turbulent fluctuations above the buffer layer of wall-bounded flows, *Journal of Fluid Mechanics*, **611**, 2008, 215–236.

[16] Katul, G. and Vidakovic, B., The partitioning of attached and detached eddy motion in the atmospheric surface layer using Lorentz wavelet filtering, *Boundary-Layer Meteorology*, **77**, 1996, 153–172.

[17] Kunkel, G. J. and Marusic, I., Study of the near-wall-turbulent region of the high-Reynolds-number boundary layer using an atmospheric flow, *Journal of Fluid Mechanics*, **548**, 2006, 375–402.

[18] Lee, M. and Moser, R. D., Direct numerical simulation of turbulent channel flow up to $Re_\tau \approx 5200$, *Journal of Fluid Mechanics*, **774**, 2015, 395–415.

[19] Marusic, I., Chauhan, K., Kulandaivelu, V. and Hutchins, N., Evolution of zero-pressure-gradient boundary layers from different tripping conditions, *Journal of Fluid Mechanics*, **783**, 2015, 379–411.

[20] Marusic, I., Mathis, R. and Hutchins, N., Predictive model for wall-bounded turbulent flow, *Science*, **329**, 2010, 193–196.

[21] Marusic, I. and Monty, J. P., Attached eddy model of wall turbulence, *Annual Review of Fluid Mechanics*, **51**, 2019, 49–74.

[22] Marusic, I., Monty, J. P., Hultmark, M. and Smits, A. J., On the logarithmic region in wall turbulence, *Journal of Fluid Mechanics*, **716**, 2013, R3.

[23] Mathis, R., Hutchins, N. and Marusic, I., Large-scale amplitude modulation of the small-scale structures in turbulent boundary layers, *Journal of Fluid Mechanics*, **628**, 2009, 311–337.

[24] Morrison, J. F., The interaction between inner and outer regions of turbulent wall-bounded flow, *Philosophical Transactions of the Royal Society A: Mathematical, Physical and Engineering Sciences*, **365**, 2007, 683–698.

[25] Morrison, J. F., Subramanian, C. S. and Bradshaw, P., Bursts and the law of the wall in turbulent boundary layers, *Journal of Fluid Mechanics*, **241**, 1992, 75–108.

[26] Orlandi, P., Bernardini, M. and Pirozzoli, S., Poiseuille and Couette flows in the transitional and fully turbulent regime, *Journal of Fluid Mechanics*, **770**, 2015, 424–441.

[27] Panton, R. L., Composite asymptotic expansions and scaling wall turbulence, *Philosophical Transactions of the Royal Society A: Mathematical, Physical and Engineering Sciences*, **365**, 2007, 733–754.

[28] Perry, A. and Chong, M., On the mechanism of wall turbulence, *Journal of Fluid Mechanics*, **119**, 1982, 173–217.

[29] Perry, A., Henbest, S. and Chong, M., A theoretical and experimental study of wall turbulence, *Journal of Fluid Mechanics*, **165**, 1986, 163–199.

[30] Prandtl, L., Bericht über untersuchungen zur ausgebildeten turbulenz, *ZAMM*, **5**, 1925, 136–139.

[31] Saddoughi, S. G. and Veeravalli, S. V., Local isotropy in turbulent boundary layers at high Reynolds number, *Journal of Fluid Mechanics*, **268**, 1994, 333–372.

[32] Sillero, J. A., Jiménez, J. and Moser, R., Two-point statistics for turbulent boundary layers and channels at Reynolds numbers up to $\delta^+ \approx 2000$, *Physics of Fluids*, **26**, 2014, 105109.

[33] Tinney, C., Coiffet, F., Delville, J., Hall, A., Jordan, P. and Glauser, M., On spectral linear stochastic estimation, *Experiments in Fluids*, **41**, 2006, 763–775.

[34] Townsend, A., *The structure of turbulent shear flow*, Cambridge University Press, 1976, 2nd edn. Cambridge University Press edition.

[35] Townsend, A. A., Equilibrium layers and wall turbulence, *Journal of Fluid Mechanics*, **11**, 1961, 97–120.

[36] Wu, S., Christensen, K. and C., P., Modelling smooth- and transitionally rough-wall turbulent channel flow by leveraging inner–outer interactions and principal component analysis, *Journal of Fluid Mechanics*, **863**, 2019, 407–453.

[37] Yoon, M., Hwang, J., Yang, J. and Sung, H. J., Wall-attached structures of streamwise velocity fluctuations in an adverse-pressure-gradient turbulent boundary layer, *Journal of Fluid Mechanics*, **885**, 2020, A12.